

# Elastic anisotropy of D'' predicted from global models of mantle flow

A. M. Walker,<sup>1</sup> A. M. Forte,<sup>2</sup> J. Wookey,<sup>1</sup> A. Nowacki<sup>1</sup> and J.-M. Kendall<sup>1</sup>

An edited version of this paper was published by AGU. Copyright (2011) American Geophysical Union Walker, A. M., A. M. Forte, J. Wookey, A. Nowacki, and J.-M. Kendall (2011), Elastic anisotropy of D'' predicted from global models of mantle flow, *Geochem. Geophys. Geosyst.*, 12, Q10006, doi:10.1029/2011GC003732. To view the published open abstract, go to <http://dx.doi.org> and enter the DOI.

---

<sup>1</sup>School of Earth Sciences, University of  
Bristol, Wills Memorial Building, Queen's  
Road, Bristol, BS8 1RJ, UK.

<sup>2</sup>GEOTOP - Dépt. Sci. Terre &  
Atmosphère, Université du Québec à  
Montréal, CP 8888 succursale Centre-Ville,  
Montréal QC, H3C 3P8, Canada.

**Abstract.** In order to test the hypothesis that seismic anisotropy in the lowermost mantle is caused by the development of a post-perovskite lattice preferred orientation, and that anisotropy can thus be used as a probe of the dynamics of the mantle's lower boundary layer, an integrated model of texture generation in D'' is developed. This is used to predict the elastic anisotropy of the lowermost mantle as probed by global anisotropic tomographic inversions. The model combines the current 3D mantle flow field with simulations of the deformation of post-perovskite polycrystalline aggregates. Different descriptions of single crystal plasticity can lead to model results which are anti-correlated to each other. In models where post-perovskite deformation is accommodated by dislocations moving on (010) or (100), patterns of anisotropy are approximately correlated with the results of tomographic inversions. On the other hand, in models where dislocations move on (001) patterns of anisotropy are nearly anti-correlated with tomographic inversions. If all the seismic anisotropy extracted from global anisotropic inversions is due to the presence of a lattice preferred orientation in post-perovskite in the lowermost mantle, and if the results of the tomographic inversions are not strongly biased by the sampling geometries, these results suggest that, in contrast to ideas based on the 1D anisotropic signal, deformation of post-perovskite in the lowermost mantle may be accommodated by dislocations moving on (010) or (100). Alternatively, a significant portion of the anisotropic signal may be caused by mechanisms other than the alignment of post-perovskite crystals.

## 1. Introduction

Unlike the majority of the lower mantle the lowermost layer, known as D'', exhibits significant seismic anisotropy. Measurements of shear wave splitting from ScS, SKS and Sdiff phases which pass through D'' in particular places demonstrate that, at least in some areas, the region above the core mantle boundary (CMB) is anisotropic [e.g. *Lay and Young*, 1991; *Vinnik et al.*, 1995; *Kendall and Silver*, 1996; *Wookey et al.*, 2005a; *Rokosky et al.*, 2006; *Wookey and Kendall*, 2007; *Long*, 2009; *Nowacki et al.*, 2011]. The anisotropy extracted from studies of normal mode data suggests that, on average, a horizontally polarised S-wave propagating parallel to the CMB will travel more quickly than a vertically polarised S-wave following the same path [*Montagner and Kennett*, 1996], but a more recent analysis suggests that an isotropic layer would also fit the data [*Beghein et al.*, 2006]. Global scale inversions of body S-wave data including the effect of anisotropy reveal an anisotropic layer at the base of the mantle but, beyond the broadest scale features, the detailed patterns of the anisotropy are not robustly reproduced between studies [*Panning and Romanowicz*, 2004, 2006; *Kustowski et al.*, 2008]. Increasing anisotropy with depth is also a feature of the lowermost mantle as imaged by P-wave tomography where vertically and horizontally propagating waves are treated separately [*Boschi and Dziewonski*, 2000; *Soldati et al.*, 2003]. However, there is an important trade-off in these studies making it hard to unambiguously distinguish an anisotropic lower mantle from a heterogeneous outer core. One explanation for the anisotropy of D'', which has become increasingly prominent since the discovery of the perovskite to post-perovskite phase transition in the MgSiO<sub>3</sub> system, is that it is caused by a deformation-induced lattice preferred orientation

(LPO) in the lower boundary layer of the convecting mantle. If this is the case, the observation of anisotropy in the lowermost mantle could be used as a probe of dynamics in this complex region [e.g. *Panning and Romanowicz, 2004; Merkel et al., 2007*].

The origin of the anisotropy observed in the lowermost mantle has been the subject of considerable debate. In the context of the observation of shear wave splitting in SKS and SKKS phases, *Hall et al. [2004]* enumerated several possibilities: the anisotropy could be caused by the alignment of solid or melt-filled inclusions in an isotropic matrix (types of shape preferred orientation, SPO) or by the orientation of individual elastically anisotropic crystals defining an LPO. In the latter case, *Hall et al. [2004]* considered the possible alignment of MgSiO<sub>3</sub> perovskite, periclase, and columbite structured SiO<sub>2</sub>. *Wenk et al. [2006]* simulated LPO development in a subducting slab consisting of ferropericlase and MgSiO<sub>3</sub> perovskite and predicted the development of significant anisotropy above the CMB. Since its discovery, attention has focused on MgSiO<sub>3</sub> post-perovskite. Because post-perovskite is believed to be more abundant than periclase and more anisotropic than perovskite, a weaker LPO is needed to yield the same strength of anisotropy.

LPO development is a product of deformation accommodated by dislocation glide in a polycrystalline sample. Because each crystal deforms by the motion of dislocations in specific glide planes, the crystal lattice will tend to rotate such that the easy slip plane(s) align parallel to the extension direction or shear plane. This single crystal response is mediated by the need to maintain equilibrium and compatibility across the grain boundaries (the stresses must balance and the grains cannot overlap) and eventually limited by dynamic recrystallisation or grain size reduction and the onset of diffusion controlled deformation. Significant effort has been expended to establish the deformation mecha-

nism, rheology, and active slip planes in  $\text{MgSiO}_3$  post-perovskite. In-situ experiments in the diamond anvil cell suggest a combination of slip on (100) and {110} [Merkel *et al.*, 2007] or slip on (001) [Miyagi *et al.*, 2010]. Experiments on analogues, principally  $\text{CaIrO}_3$  but also  $\text{CaPtO}_3$ , tend to favour slip on (010) [Yamazaki *et al.*, 2006; Niwa *et al.*, 2007; Walte *et al.*, 2007, 2009; Miyagi *et al.*, 2008; Miyajima *et al.*, 2010; McCormack *et al.*, In Press] but other slip systems have been reported for the  $\text{Mn}_2\text{O}_3$  and  $\text{MgGeO}_3$  analogues [Santillán *et al.*, 2006; Merkel *et al.*, 2006; Okada *et al.*, 2010; Hirose *et al.*, 2010]. An alternative approach, taken by Carrez *et al.* [2007a, b] and Metsue *et al.* [2009], is to study the resistance to dislocation motion using the Peierls–Nabarro model parameterised by atomic scale simulations using density functional theory (DFT). These calculations suggest that, if dislocation motion is rate limited by the Peierls barrier [see Walker *et al.*, 2010], (010) should be the easy slip plane for  $\text{MgSiO}_3$  and  $\text{CaIrO}_3$  post-perovskite.

Consideration of the single crystal elastic properties of post-perovskite along with the globally averaged anisotropy pattern has been used to argue that (001) in post-perovskite is aligned parallel to the CMB, as horizontally polarised shear waves are then faster than vertically polarised waves for all azimuths. When combined with the expectation that flow in the lowermost mantle should be dominantly horizontal, this suggests that the easy-slip systems should involve dislocations gliding on (001) [Wookey *et al.*, 2005b; Wookey and Kendall, 2007; Miyagi *et al.*, 2010; Okada *et al.*, 2010]. In the current work we seek to begin to test the hypothesis that the observed global scale pattern of seismic anisotropy is caused by the development of a deformation-induced LPO in post-perovskite and, if this is the case, to understand which slip systems are most active in the deforming lowermost mantle. We follow the same general approach that has been used for studies of the upper

mantle to couple large-scale models of mantle deformation with numerical simulations of texture development [e.g. *Blackman et al.*, 1996, 2002; *Wenk and Tomé*, 1999; *Tommasi et al.*, 1999, 2000; *Kaminski and Ribe*, 2001; *Blackman and Kendall*, 2002; *Kaminski et al.*, 2004; *Becker et al.*, 2008]. In this study, global models of present-day mantle flow are used to drive the simulation of LPO development as material transits D''. The predicted textures are used to generate models of elastic anisotropy and these are compared with the anisotropic S-wave inversions of *Panning and Romanowicz* [2006], *Kustowski et al.* [2008] and *Panning et al.* [2010] and the anisotropic P-wave tomography of *Soldati et al.* [2003]. Uncertainty in the single crystal slip system activities and present-day flow model are explored by including a range of plausible models in each case. In examining the effect of post-perovskite alignment on seismic anisotropy we choose to neglect the possible effect of point-defect accommodated deformation, the alignment or segregation of other phases and small scale structures such as layering and the inclusion of melt pockets. Our approach differs from previous work intended to simulate the development of LPO in the lowermost mantle in two ways [*Wenk et al.*, 2006; *Merkel et al.*, 2007; *Wenk et al.*, 2011]. Firstly, our mantle flow field is derived from the inversion of seismic and geodynamic data rather than from a general circulation model. This permits direct comparison between the distribution of modelled LPO and seismic observations. Secondly, previous work made use of two dimensional (2D) models of flow while the current flow field is three dimensional (3D) eliminating an important uncertainty in evaluating the results [*Wenk et al.*, 2011].

## 2. Methodology

The approach taken to calculate the elastic anisotropy of D'' is illustrated in Figure 1. Our starting point is a model of current mantle flow. For this we use predictions

of mantle convective flow calculated on the basis of density anomalies obtained in joint inversions of S-wave travel times and geodynamic data [Simmons *et al.*, 2007, 2009]. Using this flow model as input, we trace the pathlines followed by packets of material moving through the post-perovskite stability field. We calculate the velocity gradient tensor at steps along each pathline and use these as the boundary conditions for the calculation of the textural evolution of post-perovskite aggregates. The calculated textures are then used to calculate the aggregate elastic constants for the deformed polycrystal along with key parameters summarising the anisotropy. These parameters are then compared with seismic observations.

## 2.1. Flow Model

The flow models are based on the joint inversion of global S-wave travel times, the global gravity field, dynamic surface topography, tectonic plate motions, and of the excess ellipticity of the core-mantle boundary undertaken by Simmons *et al.* [2007, 2009]. Key to the joint inversion process is the use of realistic parameters taken from mineral physics to convert from S-wave velocity to density and the inversion produces a 3D model of mantle density perturbations which are decomposed into thermal and non-thermal (compositional) contributions. An additional input to the mantle flow calculations is the use of geodynamically-consistent mantle viscosity profiles that provide an optimal fit to both glacial-isostatic adjustment (GIA) and mantle convection data sets [Mitrovica and Forte, 2004, Figure 2]. Two density models derived from the joint seismic-geodynamic inversion are used and they are termed TX2007 and TX2008. The TX2008 model [Simmons *et al.*, 2009] is smoother than the TX2007 model [Simmons *et al.*, 2007]. The thermal and non-

thermal contributions to the density anomalies in these two models for the lowermost 240 km of the mantle are contrasted in Figure 3.

We employ a theory of viscous flow in a compressible, self-gravitating spherical mantle with coupled surface plate motions [Forte, 2007] to calculate the mantle convective flow predicted on the basis of the tomographically-inferred 3D density anomalies. In these flow calculations we employ two viscosity profiles, respectively termed V1 and V2 (Figure 2), that are derived from the joint GIA-convection inversions [Mitrovica and Forte, 2004]. Both viscosity profiles are characterised by a three-order of magnitude increase of viscosity from the base of the lithosphere down to the middle of the lower-mantle, with a subsequent rapid decrease of viscosity in the lowermost mantle. The main difference between these two viscosity models is presence of a strong reduction in viscosity in a thin layer at the base of the upper mantle in V1 and a somewhat stiffer lower-mantle viscosity in V2. The different combinations of mantle viscosity and 3D density models yield a total of four possible flow models (Figure 4) that we employ to carry out the calculations of texture development.

## 2.2. Pathline Construction

To calculate the texture and elastic constants at a particular location from a flow model it is necessary to track the path taken by a particle of material before it arrived at the chosen location and evaluate the strain imposed during the traversal of the path. The quantity needed, at each step along the path, is the velocity gradient tensor,  $\mathbf{L}$ , given by the rate of change in the velocity vector,  $\mathbf{v}$ , with position,  $\mathbf{x}$ :

$$L_{ij} = dv_i/dx_j. \quad (1)$$

This asymmetric second rank tensor can be decomposed into a symmetric part, which is the strain rate tensor,  $\dot{\mathbf{E}}$ :

$$\dot{E}_{ij} = (L_{ij} + L_{ji})/2, \quad (2)$$

and a skew-symmetric part, which is the rotation rate tensor,  $\dot{\Omega}$ :

$$\dot{\Omega}_{ij} = (L_{ij} - L_{ji})/2. \quad (3)$$

The task is to calculate, on a global basis, a sequence of velocity gradient tensors along the paths taken by particles which sample D'' for each flow model and then, for each particle, simulate the generation of texture and thus seismic anisotropy. In the current work, paths in D'' are selected to end on a regular  $5^\circ$  by  $5^\circ$  latitude (*lat*) longitude (*lon*) grid 75 km above the CMB (*R*).

Taking inspiration from the D-Rex program [Kaminski *et al.*, 2004], and advantage of the fact that the flow fields are, for the current simulations, assumed not to change with time, particles are tracked backwards in time from the location inside the post-perovskite stability field where the elastic constants are desired to the point where the pathline crosses the perovskite to post-perovskite phase boundary. (As discussed below, this approach involves an assumption that the phase transition will reset any pre-existing texture.) The approach to find the pathline involves first converting geographical coordinates (*R*, *lat*, *lon*) at time,  $t = t_0$ , to coordinates on a global Cartesian reference frame,  $\mathbf{x}_{t_0}$ . The velocity gradient tensor,  $\mathbf{L}_{t_0}$ , at  $\mathbf{x}_{t_0}$  is calculated using an adaptive finite differencing approach and stored. The position of the particle at an earlier time,  $t_1 = t_0 - \Delta t$ , is then found by fourth order Runge-Kutta integration through the reversed velocity field and stored. This procedure is then repeated to generate a list of velocity gradient tensors ( $\mathbf{L}_{t_0}, \mathbf{L}_{t_1}, \dots, \mathbf{L}_{t_N}$ )

corresponding to locations on the pathline ( $\mathbf{x}_{t_0}, \mathbf{x}_{t_1}, \dots, \mathbf{x}_{t_N}$ ). Once the pathline extends outside the post-perovskite stability field the process is stopped and the lists are reversed so they can be used as input for the simulation of texture generation. A 25,000 year time step separates the points on the pathline. This choice of time step generates paths which are very similar to those generated with a shorter (15,000 year) time step.

Two approaches are used to define the perovskite to post-perovskite phase boundary, terminate the generation of the pathline, and locate the starting point for the simulation of texture development. The first approach is to set the phase transition to a fixed height 150 km above the CMB (the thickness of D'' in PREM). This is equivalent to assuming the Clapeyron slope for the perovskite to post-perovskite phase transition is flat and so that, at least in the relevant region of pressure–temperature space, the transition pressure is independent of temperature. The stop condition for the pathline generation is then implemented by comparing the height of the particle above the CMB with the chosen stop height at each step. The second approach seeks to maximise the topography on the phase transition. Parameters for the Clapeyron slope are taken from the DFT calculations within the generalised gradient approximation which give a slope of  $9.56 \text{ MPaK}^{-1}$  and 0 K transition pressure of 98.7 GPa [Oganov and Ono, 2004]. Subsequent calculations and experiments suggest that this is a reasonable upper bound for the Clapeyron slope (*Tsuchiya et al.* [2004] and *Hirose et al.* [2006] both give smaller values) and, when combined with the thermal model described below, this choice of parameters gives a good match to the depth of the D'' reflector observed under Siberia [*Thomas et al.*, 2004]. The presence of a non-zero Clapeyron slope combined with the likelihood of a non-linear geotherm close to the CMB offers the intriguing possibility of double crossings of the phase boundary with

depth in relatively cold regions of the lowermost mantle and no post-perovskite in hot regions [Hernlund *et al.*, 2005]. This possibility is included in the pathline construction by building a simple thermal model of the lowermost mantle which is consistent with the thermal anomalies predicted from the density inversions. The 1D geotherm of *Stacey and Davis* [2008] is used and perturbed at each geographical location by the thermal anomaly from the joint seismic-geodynamic inversion being used to produce the flow model to give the total estimated temperature at the point being considered during the construction of the pathline. This is used with the parameters describing the phase transition to determine if the point is inside the post-perovskite stability field and, if it is not, construction of the pathline is terminated. Note that this approach permits double crossings of the phase boundary. Where these are present, the pathline for a particle in an upwelling (being tracked backwards towards the CMB) can terminate on the deeper post-perovskite to perovskite phase boundary. However, the majority of paths terminate normally at the upper perovskite to post-perovskite boundary encountered in a downwelling (when the particle is being tracked backwards away from the CMB).

### 2.3. Textural Evolution

Single crystal deformation of post-perovskite is assumed to be due to the motion of dislocations on specific glide planes. The choice of available glide planes and Burgers vectors results in the specification of  $s$  slip-systems, each of which can contribute to the local (grain-scale) strain. The strain rate contribution of each slip system,  $\dot{\gamma}^s$ , is determined by the resolved shear stress on the slip system,  $\tau_r^s$ , a reference yield stress for

the slip system,  $\tau_0^s$ , a stress exponent,  $n^s$  and a reference strain rate,  $\dot{\gamma}_0$ :

$$\dot{\gamma}^s = \dot{\gamma}_0 \left( \frac{\tau_r^s}{\tau_0^s} \right)^{n^s}. \quad (4)$$

If the orientation of the slip system is defined by unit vectors for the Burgers vector direction,  $\hat{\mathbf{b}}^s$ , and pole to the slip plane,  $\hat{\mathbf{n}}^s$ , expressed on the global Cartesian reference frame, the crystal strain rate tensor,  $\dot{\varepsilon}$ , and plastic rotation rate tensor,  $\dot{\omega}^p$ , can be found by summing the contributions from each slip system:

$$\dot{\varepsilon}_{ij} = \sum_s \dot{\gamma}^s \frac{1}{2} \left( \hat{b}_i^s \hat{n}_j^s + \hat{b}_j^s \hat{n}_i^s \right), \quad \dot{\omega}_{ij}^p = \sum_s \dot{\gamma}^s \frac{1}{2} \left( \hat{b}_i^s \hat{n}_j^s - \hat{b}_j^s \hat{n}_i^s \right). \quad (5)$$

The single crystal slip-system parameters used in this study are summarised in Table 1 and are intended to reproduce a range of possibilities suggested by experiments and atomic scale simulations. In particular, we include the parameter sets previously used for texture modelling by *Merkel et al.* [2007] and *Metsue et al.* [2009] favouring (100) / {110} and (010), respectively, and add a set of slip system parameters intended to reproduce the (001) texture found by *Miyagi et al.* [2010]. Models derived from these parameters are named P100, P010 and P001 (Table 1).

LPO formation involves the rotation and alignment of a population of crystals in a polycrystalline aggregate. Rather than attempting to explicitly describe all interactions between adjacent crystals, texture development in the polycrystalline aggregates are modelled using the visco-plastic self-consistent (VPSC) approach of *Lebensohn and Tomé* [1993] where interactions between grains are represented by embedding each grain in a homogeneous effective medium representing the other grains in the sample. Briefly, this approach involves the calculation of the stress and strain rate ( $\sigma, \dot{\varepsilon}$ ) in each grain based on the assumption that their volume averages equal the macroscopic stress and strain

rate ( $\Sigma, \dot{\mathbf{E}}$ ). Each grain is assumed to be ellipsoidal and the behaviour of the surrounding homogeneous effective medium is taken as the weighted average of the behaviour of all the grains in the sample. This leads to:

$$\dot{\varepsilon}_{ij} - \dot{E}_{ij} = -\alpha M_{ijkl}(\sigma_{kl} - \Sigma_{kl}), \quad (6)$$

where  $M$  is the tensor describing the interaction which depends on the rheology of the aggregate and the ellipticity of the grains,  $\alpha$  is a parameter describing the interaction between the grains and the effective medium. ( $\alpha = 0$  yields the Taylor model where the strain in each crystal is equal and increasing  $\alpha$  makes the stress in each crystal more similar. In the current work  $\alpha = 1$ , which gives the tangent model of *Lebensohn and Tomé* [1993].) Full details of the self-consistent solution to this model are given in *Lebensohn and Tomé* [1993] and *Tomé and Canova* [1998]. Once a solution has been found  $\dot{\omega}^p$  is calculated for each grain. The total rotation,  $\dot{\omega}$ , of each grain is calculated from  $\dot{\omega}^p$ ,  $\dot{\Omega}$ , and the reorientation rate of the associated ellipsoidal inclusion,  $\dot{\omega}^r$ :

$$\dot{\omega}_{ij} = \dot{\Omega}_{ij} - \dot{\omega}_{ij}^p + \dot{\omega}_{ij}^r. \quad (7)$$

$\dot{\omega}^r$  depends on the difference in strain rate between the grain and the polycrystal, and increases as the grain becomes more ellipsoidal.

The VPSC approach allows the calculation of texture development in D''. A sample of 500 randomly orientated spherical grains is generated at the start of each pathline (i.e., we assume no texture is created during the perovskite to post-perovskite phase transition and no pre-existing texture survives the transition), and strain, given by the first of the stored velocity gradient tensors, is applied. This results in the crystals being rotated and this slightly deformed sample is subject to the next increment of strain on the next step

on the pathline. By the time the pathline ends a deformation induced texture has been imposed on the sample and this can be used for the calculation of elastic anisotropy on the global grid.

## 2.4. Elastic constants

The texture calculated at each grid point is represented by 500 individual crystal orientations each denoted by three Euler angles,  $(\varphi_1, \Phi, \varphi_2)$ , describing the rotation of the crystal from the common global Cartesian frame. The elastic stiffness tensor of the aggregate is calculated by Voigt-Reuss-Hill averaging of the single crystal elastic stiffness tensor,  $\mathbf{c}(p, t)$ , and compliance tensor,  $\mathbf{s}(p, t) = \mathbf{c}^{-1}(p, t)$ , at the pressure,  $p$ , and temperature,  $t$ , from the perturbed geotherm used to define the phase transition.  $\mathbf{c}(p, t)$  is found using the interpolative approach described by *Ammann et al.* [2010] where the interpolation in pressure–temperature space uses the pressure derivatives of *Wentzcovitch et al.* [2006] to extend the calculations of *Stackhouse et al.* [2005] and *Stackhouse and Brodholt* [2007]. (The effect of temperature and pressure on the single crystal anisotropy is small compared to the other factors considered in our model, but including the pressure and temperature derivatives at this point simplifies the future use of the calculated aggregate elasticities.) The Euler angles describing the orientation of each crystal are converted into a rotation matrix,  $\mathbf{g}(\varphi_1, \Phi, \varphi_2)$ . The Voigt average stiffness tensor of the aggregate,  $\tilde{\mathbf{C}}$ , is then given by averaging the elements of the rotated single crystal tensor:

$$\tilde{C}_{ijkl} = \frac{1}{500} \sum_{n=1}^{500} g_{i\alpha}^n g_{j\beta}^n g_{k\gamma}^n g_{l\delta}^n c_{\alpha\beta\gamma\delta}, \quad (8)$$

where repeated indices on the right hand side imply a summation. The Reuss average of the compliance tensor,  $\tilde{\mathbf{S}}$ , is found in a similar manner:

$$\tilde{S}_{ijkl} = \frac{1}{500} \sum_{n=1}^{500} g_{i\alpha}^n g_{j\beta}^n g_{k\gamma}^n g_{l\delta}^n s_{\alpha\beta\gamma\delta}, \quad (9)$$

and average of these two tensors is the Voigt-Reuss-Hill estimate of the elastic stiffness tensor of the aggregate,  $\mathbf{C}$ :

$$C_{ijkl} = \frac{\tilde{C}_{ijkl} + \tilde{S}_{ijkl}^{-1}}{2}. \quad (10)$$

Expressing the elastic constants on a single global axis system is rather unintuitive. To simplify comparison with global seismic observations,  $\mathbf{C}$  is rotated from the global Cartesian reference frame into a local reference frame where the X3 axis is oriented vertically, X1 points to the north pole and X2 points to the west (giving a right handed system). Elastic stiffness tensors expressed on this system are thus the primary results of the current work.

On the global scale, anisotropy is commonly assumed to exhibit hexagonal symmetry with the symmetry axis aligned vertically, a situation known as vertical transverse isotropy (VTI). This case is equivalent to the anisotropy generated by the stacking of alternating layers of stiff and soft materials on a scale much shorter than the seismic wavelength or to the elasticity exhibited by a hexagonal crystal with a vertical 6-fold rotation axis. For VTI, the elastic properties must be described by five parameters. A vertically propagating shear wave would experience no splitting and a horizontally propagating shear wave would be split into a horizontally polarised wave and a vertically polarised wave travelling at different velocities. The difference between the velocity of the horizontally polarised wave,  $V_{SH}$ , and the vertically polarised wave,  $V_{SV}$ , provides a commonly reported parameter describing the shear-wave anisotropy,  $\xi$ , defined as:  $\xi = V_{SH}^2/V_{SV}^2$ . However, no symmetry

is imposed by the steps taken to calculate  $C$  and, in general, 21 different elastic constants will be required. In order to calculate  $\xi$ ,  $C$  is rotated about the vertical axis in  $5^\circ$  steps, and the Voigt-Reuss-Hill average of each of the rotated tensors is calculated (using Equations 8 – 10 with  $\mathbf{g}$  now only being a function of one rotation angle) to give  $C^{VTI}$ . This process imposes hexagonal symmetry with a vertical symmetry axis.  $\xi$  can then be readily calculated by solving the Christoffel equation for a horizontally propagating wave.

### 3. Results

The main results of the calculations are a collection of elastic stiffness tensors globally distributed across  $D''$  for each of the flow fields and assumed single crystal plasticity models. We name these models by concatenating the names of each component (joint seismic-geodynamic inversion: “TX2007” or “TX2008”, radial viscosity profile: “V1” or “V2”, and plasticity model: “P100”, “P010” or “P001”) and include a “T” when topography on the phase transition is considered (e.g. TX2007.V1.P100 or TX2008.V2.T.P010). Values of the elastic constants for the 15 combinations considered (we only include  $D''$  topography for the TX2008.V2 flow model) are provided in machine readable format in the electronic supplementary information and are summarised, in the form of the geographically distributed  $\xi$  parameter, in Figures 5, 6 and 7, and the supplementary information. A few key parameters of these VTI models, namely the maximum, minimum and mean shear wave anisotropy and the degree to which a VTI model is appropriate (calculated using the method of *Browaeys and Chevrot [2004]*) are given in Table 2. In order to understand these data, it is useful to first consider details of the calculated pathlines.

Particle trajectories through  $D''$  are diverse: pathline lengths vary from  $\sim 6000$  to  $\sim 75$  km, sample different depths and have differing tortuosity. Particle velocities vary from

$\sim 10$  to  $\sim 0.1$  cm/year (Table 3). Particle velocities from flow models making use of the less viscous V1 viscosity model are faster than the flow models making use of the more viscous V2 viscosity model, while the range of velocities is greater for the less-smoothed TX2007 density inversion than for the smoother TX2008 inversion. The shortest paths correspond to particles which enter the post-perovskite field in a downwelling and move directly downwards to the sampling depth. For the case of a perovskite to post-perovskite phase transition at a constant depth 150 km above the CMB these paths are thus 75 km long and have a tortuosity of 1. In the case of strong topography on the phase transition the shortest paths need not be directly downwards and can be arbitrarily short. In our model, these shortest pathlines have the least time to develop texture and thus give small anisotropies. Temperature induced topography on the perovskite to post-perovskite transition depth results in reducing the length of the longest and shortest pathlines but makes little difference to the mean pathline length.

Differences in the flow models and calculated pathlines result in differences in the calculated elastic constants and  $\xi$  distributions. The more viscous models generate larger anisotropy over wider areas (Figure 6) than the less viscous models where the anisotropy is less intense over much of the globe (Figure 5). Smoothing of the density model has a modest effect as shown in the supplementary information. These effects, however, pale into insignificance when compared to differences generated by changing the model of the single crystal plasticity of post-perovskite. The same general differences between plasticity models can be seen whatever flow model is used for the calculation (this is even the case for the shortest pathlines in downward flowing material under New Zealand and South America, which shows the initial random texture is rapidly removed). As expected from

consideration of the single crystal elasticity, the anisotropy from models favouring slip on (001) planes (part b of Figures 5 and 6) is generally anti-correlated with the anisotropy of models favouring slip on (100) and {110} (part c of Figures 5 and 6). The general pattern of anisotropy is perhaps best seen in Figure 6 which represents the smoother TX2008 joint inversion with the more viscous V2 viscosity model. The P010 and P100 plasticity models which favour slip on (010) or (100) and {110} (part a and c, respectively) show a similar pattern with positive  $\xi$  in regions of downwelling such as under South America and the northwest and southwest Pacific, and development of negative  $\xi$  in the broad regions of near horizontal flow which persists into the strongest upwellings. The P001 model favouring slip on (001) shows the opposite pattern with small regions of negative or near zero  $\xi$  around the downwellings and the development of strong positive  $\xi$  elsewhere. The P010 model based on Peierls-Nabarro modelling (part a of Figures 5 and 6) always exhibits the weakest anisotropy but has a spatial pattern that is similar to the P100 models. The weaker texture developed in the models from the Peierls-Nabarro results (P010) is due to the lower anisotropy of the single crystal yield surface for these parameters. Multiple relatively weak slip systems can carry strain which reduces the plastic rotation of the crystals in the VPSC simulation.

Comparing Figures 6 and 7 shows that, away from the areas of elevated temperature under the Pacific and southern Africa, the effect of imposing temperature induced topography on the phase transition is minor. In these hottest areas the thermal model implies that there will be no post-perovskite at the sampling depth removing any anisotropic signal from post-perovskite deformation in our models (the green areas in Figure 7). However, we note that this does not rule out anisotropy caused by the alignment of post-perovskite

in these regions as post-perovskite can exist closer to the CMB. Away from these holes in our models, the pattern of anisotropy is nearly unaffected by the change in thickness of the post-perovskite layer. This insensitivity is due to the fact that the change in path length is generally small, and removing the ends of paths in hot upwellings cannot change the texture earlier on the pathline.

In the supplementary information and Figure 8, we present maps the parameter  $\ln(\phi)$ , which describes the P-wave anisotropy ( $\phi = V_{PV}^2/V_{PH}^2$ , where  $V_{PV}$  and  $V_{PH}$  are the velocities of vertically and horizontally propagating P-waves in a VTI medium, respectively). Unsurprisingly, it turns out that  $\ln(\phi)$  is strongly correlated to, or anti-correlated to,  $\ln(\xi)$  for all our models with the sign of the correlation depending on the most active slip system. When slip is accommodated on (010) or (001)  $\ln(\phi)$  and  $\ln(\xi)$  are correlated but the two parameters are anti-correlated if (100) is the dominant plane. (Essentially,  $\ln(\xi)$  is positive if the [001] axis is a vertically oriented axis of symmetry and negative otherwise;  $\ln(\phi)$  is negative if [010] is a vertically oriented axis of symmetry and positive otherwise [Stackhouse *et al.*, 2005].) If the lowermost mantle does exhibit VTI symmetry generated by the alignment of post-perovskite crystals this correlation could provide a diagnostic fingerprint, as discussed below.

#### 4. Discussion

The key assumption of the modelling described above is that all anisotropy in D" is due to the presence of a preferred alignment of post-perovskite crystals which is formed by the deformation accompanying mantle convection. If this process is the cause of the observed anisotropy of the lowermost mantle, and if any of the assumed flow fields and models of single crystal plasticity are reasonably accurate descriptions of the conditions in D", a

comparison between the observed anisotropy and the predictions of the current models should yield insight on both the single crystal plasticity and on flow in the lowermost mantle.

There are many seismic datasets which could be used for this comparison but given the global nature of our results we choose to focus on anisotropy found in the global anisotropic inversions of *Panning and Romanowicz* [2006], *Kustowski et al.* [2008] and *Panning et al.* [2010], reproduced in Figure 9. Before describing any detailed comparisons between the present models and the tomography, it is worth noting that the tomographic inversion of anisotropy is an imperfect “ongoing experiment” with relatively weak correlation between the inversions [*Kustowski et al.*, 2008]. This may be partly explained by the use of different data sets and methodologies but other issues are also significant. Neither tomographic approach is designed to capture the potentially complex finite frequency effects which are expected in regions where the anisotropy changes (for example, modelling of SKS propagation in the upper mantle and crust shows frequency dependent changes in the recovered shear wave splitting parameters associated with both slowly [*Rümpker et al.*, 1999] and rapidly [*Hammond et al.*, 2010] varying changes in the strength and orientation of anisotropy). Furthermore, there is a potentially important trade-off between the isotropic shear wave speed anomalies and the anisotropic parameters which *Kustowski et al.* [2008] show could account for 1/3 of the anisotropic signal at the base of the mantle. Finally, the choice of crustal model [*Ferreira et al.*, 2010], and crustal correction strategy [*Panning et al.*, 2010], plays a large role in determining the apparent anisotropy. In any case, we may expect any tomographic inversion to return a signal which is smoother and of a lower amplitude than the anisotropy variation present in the lowermost mantle. We also

perform comparisons with the global anisotropic P-wave inversion of [Soldati *et al.*, 2003, Figure 10], who used the method of *Boschi and Dziewonski* [2000] with improved event locations. A major challenge in interpreting this data is that different ray paths must be used to constrain  $V_{PV}$  and  $V_{PH}$ . In the lowermost mantle  $V_{PV}$  is mostly constrained by core phases such as PKP. This means that there is a trade-off between anisotropy in the mantle and an inhomogeneous core, CMB topography must be included in the inversion, there is limited resolution in many areas, and the resolution of  $V_{PV}$  and  $V_{PH}$  are not necessarily the same. We choose a P-wave anisotropy model [SBP03; Soldati *et al.*, 2003] where the core is assumed to be homogeneous, which should tend to maximise the anisotropy in the mantle.

The most dramatic difference between the anisotropy found in global tomography (Figure 9) and the modelling results (Figures 5 – 7) is that the strength of the observed anisotropy ( $\ln(\xi)$  up to 5%) is much weaker than the modelled anisotropy ( $\ln(\xi)$  up to 29%). While some of this effect is due to the spatial smoothing of the observations, and the differences in the mean anisotropy is much smaller (Table 2), the major effect is due to several limitations in the modelling. The first missing ingredient in our model is any mechanism other than dislocation motion in post-perovskite to accommodate strain. As an example, *Merkel et al.* [2007] assume that only 10% of the strain is accommodated by dislocation glide in post-perovskite with the remaining strain accommodated by mechanisms such as point defect migration or dislocation climb, which do not contribute to the post-perovskite anisotropy. A second issue is that we do not account for the presence or deformation of ferropericlase or any other minor component in the calculation of the elastic anisotropy. If these were isotropic the effect would be to weaken the anisotropic signal

by an amount proportional to the volume fraction of the isotropic component. However, if ferropericlase were to develop a strong texture, depending on the orientation, it could strengthen or weaken the anisotropy of the aggregate. A third issue is that the model of plastic deformation does not include any mechanism to limit the maximum strength of the texture. For example, in a real crystal plastic deformation by dislocation glide is expected to increase the dislocation density (e.g. by the operation of Frank-Read sources) and thus the elastic energy stored in the crystal [see *Hull and Bacon*, 1984]. This leads the preferential formation of low angle grain boundaries and dynamic recrystallisation in the most strongly deformed grains, effectively capping the maximum strength of the texture. Entanglement of dislocations leading to strain hardening is also expected to be most important in the most rapidly deforming (and thus rotating) grains. This process will also tend to limit the generation of texture and thus limit the formation of anisotropy. These effects could be included in the current model on an ad-hoc basis by either scaling the strain extracted from the pathline construction, or by diluting the calculated anisotropy in the Voigt-Reuss-Hill averaging step. However, this approach would require the determination of an absolute anisotropy at high resolution at some reference point in D" and would involve convolving the texture-limiting effects with the uncertainty in the anisotropy of the single crystal yield surface. Instead of attempting to apply an ad-hoc solution we choose to focus on the patterns of texture development, which we believe will be less strongly affected by the missing processes than the strength of the anisotropy.

Correlation between the anisotropy predicted by the models and the results of the inversions is investigated by calculating the spherical harmonic correlation spectra for each of the models correlated with each of the tomographic inversions. The anisotropy is first

expanded as a set of spherical harmonic coefficients describing the global tomography and the model results, with the series truncated at degree  $\ell = 8$ . The power spectrum and cross power spectrum are then used to calculate the degree by degree correlation spectra [e.g. *Pauer et al.*, 2006] shown in Figure 11. This shows that correlation between the three tomographic inversions is good for low spherical harmonic degree (long wavelength features) and that this begins to tail off for higher spherical harmonic degree (shorter wavelength features). Our models show various patterns of correlation with the single crystal plasticity model playing a greater role than the flow model. Models favouring slip on (001) shows notable negative correlation with the SAW642AN [*Panning and Romanowicz*, 2006], SAW642ANb [*Panning et al.*, 2010] and S362WMANI [*Kustowski et al.*, 2008] inversions while the (010) Peierls-Nabarro based model shows positive correlation to beyond degree 5. This correlation is also present for deformation accommodated by slip on (100) and {110}. In the case of the P-wave anisotropy correlation is always much weaker (Figure 12) with none of the calculated models showing any real sign of correlation and a lack of correlation between the S-wave tomography and the P-wave tomography. The lack of correlation between the P- and S-wave tomographies is hard to explain if the anisotropy in both cases originates from a VTI layer in the lowermost mantle. This could be a signature of the more general anisotropy but it could also be caused by deficiencies in one or other tomographic model, for example by the contamination of the P-wave anisotropy of the mantle by variations in seismic velocities in the core.

The fact that the strongest correlation between our models and tomographic inversions is for single crystal plasticity favouring (010) or (100) and {110} slip is intriguing. Both normal mode data and the tomography suggest that, on average, horizontally polarised

shear waves lead vertically polarised shear waves in the lowermost mantle, giving a small positive value for  $\ln(\xi)$ . Examination of the single crystal elastic constants tensor of post-perovskite shows that this is expected when (001) is parallel to the CMB. Combined with the expectation of a dominantly horizontal flow regime in D'', these considerations have been used to suggest easy-slip on (001) is likely [e.g. *Stackhouse et al.*, 2005; *Miyagi et al.*, 2010]. However, this one-dimensional view of the Earth is misleading. Regions of positive  $\ln(\xi)$  observed in anisotropic tomographic images are not where horizontal flow is expected to dominate. Horizontal flow in Figure 4 is strongest in large areas around the plume like upwellings where  $\ln(\xi)$  is negative (e.g. around the Eastern Pacific south of the equator and south and north of the upwelling under southern Africa). These are areas where material is concentrated before joining the plumes. Indeed, comparing the pattern of flow with the tomography shows that areas of strong horizontal flow correlate with the areas of negative  $\ln(\xi)$ . This funnelling of material into plumes from linear subduction features could be an important difference between the 3D flow field used here and the 2D synthetic flow model utilised by *Wenk et al.* [2011], who call for the development of more realistic 3D modelling.

It is the correlation between regions of negative  $\ln(\xi)$  in the anisotropic topography and strong horizontal flow that leads to the correlation between our P100 and P010 models and the anisotropic tomography – these models and the tomography both show negative  $\ln(\xi)$  under the Pacific and Africa. It also explains the anti-correlation between our P001 model and the tomography – the P001 model predicts strong positive  $\ln(\xi)$  in the regions of strong horizontal flow as expected from consideration of the elastic properties of post-perovskite. The observation of a correlation between the P100 and P010 models and the

anisotropic tomography should not be taken as geophysical evidence for the likely slip system in post-perovskite or the cause of D'' anisotropy without additional consideration; correlation should not be mistaken for causation and there are a number of important assumptions that must be considered:

1. The models are based on the idea that all lowermost mantle anisotropy is caused by the formation of a LPO in response to post-perovskite deformation carried by the movement of dislocations on glide planes. The deformation mechanism and deformation mechanism map for post-perovskite under lowermost mantle conditions (high pressure, high temperature, large strain and low strain rate) is essentially unknown from experiment, so the possibility of deformation being accommodated by point defect motion [e.g. *Ammann et al.*, 2010] or other mechanisms which do not link anisotropy with flow cannot be ruled out.
2. The modelled anisotropy is based on smooth flow models created from the joint inversion of seismic and geodynamical data. This implies that the flow field is spatially smooth and does not significantly vary on the timescale of the residence time of a piece of mantle within the post-perovskite stability field. Processes such as transformational weakening [*Hunt et al.*, 2009] or the formation of a critical concentration of post-perovskite in a slowly transforming mantle [*Ammann et al.*, 2010] could lead to strain being concentrated in narrow zones far below the resolution of the input flow model.
3. In comparing the model with the tomography we assume ‘good’ azimuthal coverage for the tomography. The models are inherently of low symmetry and all 21 elastic constants are permitted to differ (Table 2); VTI is imposed by averaging the full elastic tensor around the vertical axis. In terms of the tomography this approach should be equivalent

to the situation where any point in the lowermost mantle is sampled by horizontally propagating waves with good (and even) coverage of propagation direction. But, in reality, directional coverage is unlikely to be even. For example, anisotropy in D" under the middle Pacific is probably mostly constrained by seismic waves traveling from the western Pacific subduction zones to stations in north America. In this case, we should weight the radial averaging used to find  $\xi$  to favour these west - east rays over other propagation directions. However, to achieve this, it is necessary to extract the radial coverage from the tomographic inversion. In the absence of such information, imperfect coverage will tend to lead to differences between the current calculations and the tomographic inversions, even if both describe identical elastic properties of D".

It is also worth noting that the origin of the correlation is in the regions associated with low shear wave velocity under the Pacific and Africa – warm regions of D" which are least likely to contain post-perovskite and may be expected to host other sources of anisotropy such as lenses of melt.

## 5. Conclusion

By coupling global geodynamic models of mantle flow to polycrystalline simulations of the deformation of post-perovskite we have modelled the development of elastic anisotropy of the lowermost mantle. The effect of current uncertainty in the parameters describing the deformation and flow have been explored by comparing results from a range of plausible descriptions of the single crystal plasticity and mantle flow. Although the modelled anisotropy is always too strong, in some cases there is a fair correlation between the spatial pattern of S-wave anisotropy in the current models and in the tomography. Models with single crystal deformation on (010) or (100) and {110} and anisotropic seismic

tomography both have regions of fast vertically polarised shear-waves under the Pacific and southern Africa. On the other hand, single crystal deformation on (001) leads to an anisotropy pattern which is negatively correlated with the tomographic results. There are three possible reasons for this: (a) post-perovskite in the lowermost mantle deforms by the motion of dislocations on (010) or (100) and {110} and this deformation leads to the development of an LPO which is imaged seismically. (b) Lowermost mantle anisotropy is not caused by the formation of an LPO in post-perovskite but is the signature of some other sub-wavelength feature such as the alignment of long crystal axes [McCormack *et al.*, In Press], the alignment of melt pockets or layering [*Kendall and Silver*, 1996], or both [*Holtzman and Kendall*, 2010]. (c) LPO is imaged seismically but one of the assumptions used to build the current model, or to compare it with anisotropic tomography (for example, the assumption of equal azimuthal coverage and imposition of strict VTI for D'') is incorrect, and this invalidates the current predictions. It is important to note that these explanations are not exclusive (more than one can apply at once) and need not apply everywhere. For example, it may be sensible to treat the regions of negative  $\ln(\xi)$  under the Pacific and Africa differently to other areas in explanations of the origin of D'' anisotropy, as these areas are thought to be hotter and thus least likely to contain post-perovskite and most likely to contain melt. The possibility of an inhomogeneous or non-VTI anisotropy in D'' may be supported by the lack of correlation between the observed P-wave and S-wave tomography model but difficulties with the interpretation of the P-wave tomography means that this remains an area deserving of future study. Importantly, these possibilities mean that care must be taken in any attempt to interpret lowermost mantle flow on the basis of measurements of seismic anisotropy.

While the results presented here do not allow us to distinguish between the three possibilities, there are several approaches which could remove these ambiguities. One possibility is to compare the modelled anisotropy with local shear wave splitting data, especially in areas where SKS and SKKS anisotropy differs or multiple ray paths cross, allowing VTI to be distinguished from a more generally anisotropic case [*Wookey and Kendall, 2008; Long, 2009; Nowacki et al., 2010*]. A second important area would be to improve our knowledge of the single crystal and polycrystal plasticity of post-perovskite. In particular, experiments on suitable analogues providing information on the single crystal yield surface and texture evolution to large strain would be invaluable.

If current anisotropic tomography images post-perovskite LPO under the Pacific and Africa, and if the assumptions underlying our coupled model are valid, our results suggest that dislocations in post-perovskite should glide on (100) or (010). However, this scenario is not consistent with the simple idea that, given the slight positive value of  $\ln(\xi)$  globally and that horizontal flow dominates  $D''$ , (001) slip planes are likely for post-perovskite: we demonstrate that a fully 3D flow field needs to be considered to make such inferences. A clear way to begin to resolve the anomaly between the current understanding of post-perovskite deformation and  $D''$  anisotropy is to determine the extent to which regional scale shear-wave splitting results that do not imply VTI are consistent with the LPO models described here.

**Acknowledgments.** The research leading to these results has received funding from the European Research Council under the European Union's Seventh Framework Programme (FP7/2007-2013) / ERC Grant agreement n° 240473 "CoMITAC". We thank Carlos Tomé and Ricardo Lebensohn for making their VPSC code available to us and

Mark Panning and an anonymous referee for useful reviews. Calculations were carried out using the computational facilities of the Advanced Computing Research Centre, University of Bristol (<http://www.bris.ac.uk/acrc/>). Our spherical harmonic analyses were performed using the freely available software SHTOOLS (available at <http://www.ipgp.fr/~wieczor/SHTOOLS/SHTOOLS.html>).

## References

- Ammann, M. W., J. P. Brodholt, J. Wookey, and D. P. Dobson (2010), First-principles constraints on diffusion in lower-mantle minerals and a weak D'' layer, *Nature*, 465, 462 – 465, doi:10.1038/nature09052.
- Becker, T. W., B. Kustowski, and G. Ekström (2008), Radial seismic anisotropy as a constraint for upper mantle rheology, *Earth and Planetary Science Letters*, 267, 213 – 227, doi:10.1016/j.epsl.2007.11.038.
- Beghein, C., J. Trampert, and H. J. van Heijst (2006), Radial anisotropy in seismic reference models of the mantle, *Journal of Geophysical Research*, 111, B02303, doi: 10.1029/2005JB003728.
- Blackman, D. K., and J.-M. Kendall (2002), Seismic anisotropy in the upper mantle 2. Predictions for current plate boundary flow models, *Geochemistry Geophysics Geosystems*, 3, 8602, doi:10.1029/2001GC000247.
- Blackman, D. K., J.-M. Kendall, P. R. Dawson, H.-R. Wenk, D. Boyce, and J. Phipps Morgan (1996), Teleseismic imaging of subaxial flow at mid-ocean ridges: Travel-time effects of anisotropic mineral texture in the mantle, *Geophysical Journal International*, 127, 415 – 426.

Blackman, D. K., H.-R. Wenk, and J.-M. Kendall (2002), Seismic anisotropy in the upper mantle 1. Factors that affect mineral texture and effective elastic properties, *Geochemistry Geophysics Geosystems*, 3, 8601, doi:10.1029/2001GC000248.

Boschi, L., and A. M. Dziewonski (2000), Whole Earth tomography from delay times of  $P$ ,  $PcP$ , and  $PKP$  phases: Lateral heterogeneities in the outer core or radial anisotropy in the mantle?, *Journal of Geophysical Research*, 105, 13,675 – 13,698, doi:10.1029/2000JB900059.

Browaeys, J. T., and S. Chevrot (2004), Decomposition of the elastic tensor and geophysical applications, *Geophysical Journal International*, 159, 667 – 678, doi:10.1111/j.1365-246X.2004.02415.x.

Carrez, P., D. Ferré, and P. Cordier (2007a), Implications for plastic flow in the deep mantle from modelling dislocations in  $MgSiO_3$  minerals, *Nature*, 446, 68 – 70, doi:10.1038/nature05593.

Carrez, P., D. Ferré, and P. Cordier (2007b), Peierls-Nabarro model for dislocations in  $MgSiO_3$  post-perovskite calculated at 120 GPa from first principles, *Philosophical Magazine*, 87, 3229 – 3247, doi:10.1080/14786430701268914.

Ferreira, A. M. G., J. H. Woodhouse, K. Visser, and J. Trampert (2010), On the robustness of global radially anisotropic surface wave tomography, *Journal of Geophysical Research*, 115, B04313, doi:10.1029/2009JB006716.

Forte, A. M. (2007), Constraints on seismic models from other disciplines – implications for mantle dynamics and composition, in *Treatise on Geophysics. Seismology and the Structure of the Earth*, vol. 1, edited by B. Romanowicz and A. Dziewonski, pp. 805 – 858, Elsevier, doi:10.1016/B978-044452748-6.00027-4.

Hall, S. A., J.-M. Kendall, and M. van der Baan (2004), Some comments on the effects of lower-mantle anisotropy on SKS and SKKS phases, *Physics of the Earth and Planetary Interiors*, 146, 469 – 481, doi:10.1016/j.pepi.2004.05.002.

Hammond, J. O. S., J.-M. Kendall, D. Angus, and J. Wookey (2010), Interpreting spatial variations in anisotropy: insights into the Main Ethiopian Rift from SKS waveform modelling, *Geophysical Journal International*, 181, 1701 – 1712, doi:10.1111/j.1365-246X.2010.04587.x.

Hernlund, J. W., C. Thomas, and P. J. Tackley (2005), A doubling of the post-perovskite phase boundary and structure of the Earth's lowermost mantle, *Nature*, 434, 882 – 886, doi:10.1038/nature03472.

Hirose, K., R. Sinmyo, N. Sata, and Y. Ohishi (2006), Determination of post-perovskite phase transition boundary in MgSiO<sub>3</sub> using Au and MgO internal pressure standards, *Geophysical Research Letters*, 33, L01310, doi:10.1029/2005GL024468.

Hirose, K., Y. Fei, S. Merkel, and Y. Ohishi (2010), Deformation of MnGeO<sub>3</sub> post-perovskite at lower mantle pressure and temperature, *Geophysical Research Letters*, 37, 1 – 5, doi:10.1029/2010GL044977.

Holtzman, B. K., and J.-M. Kendall (2010), Organized melt, seismic anisotropy, and plate boundary lubrication, *Geochemistry Geophysics Geosystems*, 11, Q0AB06, doi:10.1029/2010GC003296.

Hull, D., and D. J. Bacon (1984), *Introduction to Dislocations*, Pergamon Press, Oxford, UK.

Hunt, S. A., D. J. Weidner, L. Li, L. Wang, N. P. Walte, J. P. Brodholt, and D. P. Dobson (2009), Weakening of calcium iridate during its transformation from perovskite

- to post-perovskite, *Nature Geoscience*, 2, 794 – 797, doi:10.1038/ngeo663.
- Kaminski, E., and N. M. Ribe (2001), A kinematic model for recrystallization and texture development in olivine polycrystals, *Earth and Planetary Science Letters*, 189, 253 – 267.
- Kaminski, E., N. M. Ribe, and J. T. Browaeys (2004), D-Rex, a program for calculation of seismic anisotropy due to crystal lattice preferred orientation in the convective upper mantle, *Geophysical Journal International*, 158, 744 – 752.
- Kendall, J.-M., and P. G. Silver (1996), Constraints from seismic anisotropy on the nature of the lowermost mantle, *Nature*, 381, 409 – 412, doi:10.1038/381409a0.
- Kustowski, B., G. Ekström, and Dziewoński (2008), Anisotropic shear-wave velocity structure of the Earth's mantle: a global model, *Journal of Geophysical Research*, 113, B06306, doi:10.1029/2007JB005169.
- Lay, T., and C. J. Young (1991), Analysis of seismic SV waves in the core's penumbra, *Geophysical Research Letters*, 18, 1373–1376.
- Lebensohn, R. A., and C. N. Tomé (1993), A self-consistent anisotropic approach for the simulation of plastic deformation and texture development of polycrystals: Application to zirconium alloys, *Acta Metallurgica et Materialia*, 41(9), 2611 – 2624, doi:10.1016/0956-7151(93)90130-K.
- Long, M. D. (2009), Complex anisotropy in D" beneath the eastern Pacific from SKS–SKKS splitting discrepancies, *Earth and Planetary Science Letters*, 283, 181 – 189, doi:10.1016/j.epsl.2009.04.019.
- McCormack, R., D. P. Dobson, N. P. Walte, N. Miyajima, T. Taniguchi, and I. G. Wood (In Press), The development of shape- and crystallographic-preferred orientation in

CaPtO<sub>3</sub> post-perovskite deformed in pure shear, *American Mineralogist*, doi:10.2138/am.2011.3881.

Merkel, S., A. Kubo, L. Miyagi, S. Speziale, T. S. Duffy, H. Mao, and H.-R. Wenk (2006), Plastic deformation of MgGeO<sub>3</sub> post-perovskite at lower mantle pressures, *Science*, 311, 644 – 646, doi:10.1126/science.1121808.

Merkel, S., A. K. McNamara, A. Kubo, S. Speziale, L. Miyagi, Y. Meng, T. S. Duffy, and H.-R. Wenk (2007), Deformation of (Mg,Fe)SiO<sub>3</sub> post-perovskite and D" anisotropy, *Science*, 316, 1729 – 1732, doi:10.1126/science.1140609.

Metsue, A., P. Carrez, D. Mainprice, and P. Cordier (2009), Numerical modelling of dislocations and deformation mechanisms in CaIrO<sub>3</sub> and MgGeO<sub>3</sub> post-perovskites — Comparison with MgSiO<sub>3</sub> post-perovskite, *Physics of the Earth and Planetary Interiors*, 174, 165 – 173, doi:10.1016/j.pepi.2008.04.003.

Mitrovica, J. X., and A. M. Forte (2004), A new inference of mantle viscosity based upon joint inversion of convection and glacial isostatic adjustment data, *Earth and Planetary Science Letters*, 225, 177 – 189, doi:10.1016/j.epsl.2004.06.005.

Miyagi, L., N. Nishiyama, Y. Wang, A. Kubo, D. V. West, R. J. Cava, T. S. Duffy, and H.-R. Wenk (2008), Deformation and texture development in CaIrO<sub>3</sub> post-perovskite phase up to 6 GPa and 1300 K, *Earth and Planetary Science Letters*, 268, 515 – 525, doi:10.1016/j.epsl.2008.02.005.

Miyagi, L., W. Kanitpanyacharoen, P. Kaercher, K. K. M. Lee, and H.-R. Wenk (2010), Slip systems in MgSiO<sub>3</sub> post-perovskite: implications for D" anisotropy, *Science*, 329, 1636 – 1638.

Miyajma, N., K. Niwa, F. Heidelbach, T. Yagi, and K. Ohgushi (2010), Deformation microtextures in CaIrO<sub>3</sub> post-perovskite under high stress conditions using a laser-heated diamond anvil cell, *Journal of Physics: Conference Series*, 215, 012097, doi: 10.1088/1742-6596/215/1/012097.

Montagner, J.-P., and B. L. N. Kennett (1996), How to reconcile body-wave and normal-mode reference Earth models, *Geophysical Journal International*, 125, 229 – 248, doi: 10.1111/j.1365-246X.1996.tb06548.x.

Niwa, K., T. Yagi, K. Ohgushi, S. Merkel, N. Miyajma, and T. Kikegawa (2007), Lattice preferred orientation in CaIrO<sub>3</sub> perovskite and post-perovskite formed by plastic deformation under pressure, *Physics and Chemistry of Minerals*, 34, 679 – 686, doi: 10.1007/s00269-007-0182-6.

Nowacki, A., J. Wookey, and J.-M. Kendall (2010), Deformation of the lowermost mantle from seismic anisotropy, *Nature*, 467, 1091 – 1094, doi:10.1038/nature09507.

Nowacki, A., J. Wookey, and J.-M. Kendall (2011), New advances in using seismic anisotropy, mineral physics and geodynamics to understand deformation in the lowermost mantle, *Journal of Geodynamics*, 52, 205 – 228, doi:10.1016/j.jog.2011.04.003.

Oganov, A. R., and S. Ono (2004), Theoretical and experimental evidence for a post-perovskite phase of MgSiO<sub>3</sub> in Earth's D'' layer, *Nature*, 430, 445 – 448.

Okada, T., T. Yagi, K. Niwa, and T. Kikegawa (2010), Lattice-preferred orientations in post-perovskite-type MgGeO<sub>3</sub> formed by transformations from different pre-phases, *Physics of the Earth and Planetary Interiors*, 180, 195 – 202, doi:10.1016/j.pepi.2009.08.002.

Panning, M., and B. Romanowicz (2004), Inferences on flow at the base of Earth's mantle based on seismic anisotropy, *Science*, 303, 351 – 353, doi:10.1126/science.1091524.

Panning, M., and B. Romanowicz (2006), A three-dimensional radially anisotropic model of shear velocity in the whole mantle, *Geophysical Journal International*, 167, 361 – 379, doi:10.1111/j.1365-246X.2006.03100.x.

Panning, M. P., V. Lekić, and B. A. Romanowicz (2010), Importance of crustal corrections in the development of a new global model of radial anisotropy, *Journal of Geophysical Research*, 115, B12325, doi:10.1029/2010JB007520.

Pauer, M., K. Fleming, and O. Cadek (2006), Modeling the dynamic component of the geoid and topography of Venus, *Journal of Geophysical Research*, 111, E11012, doi: 10.1029/2005JE002511.

Rokosky, J. M., T. Lay, and E. J. Garnero (2006), Small-scale lateral variations in azimuthally anisotropic D'' structure beneath the Cocos Plate, *Earth and Planetary Science Letters*, 248, 411 – 425, doi:10.1016/j.epsl.2006.06.005.

Rümpker, G., A. Tommasi, and J.-M. Kendall (1999), Numerical simulations of depth-dependent anisotropy and frequency-dependent wave propagation effects, *Journal of Geophysical Research*, 104, 23,141 – 23,153.

Santillán, J., S.-H. Shim, G. Shen, and V. B. Prakapenka (2006), High-pressure phase transition in Mn<sub>2</sub>O<sub>3</sub>: Application for the crystal structure and preferred orientation of the CaIrO<sub>3</sub> type, *Geophysical Research Letters*, 33, L15307, doi:10.1029/2006GL026423.

Simmons, N. A., A. M. Forte, and S. P. Grand (2007), Thermochemical structure and dynamics of the African superplume, *Geophysical Research Letters*, 34, L02,301, doi: 10.1029/2006GL028009.

Simmons, N. A., A. M. Forte, and S. P. Grand (2009), Joint seismic, geodynamic and mineral physical constraints on three-dimensional mantle heterogeneity: Implications for the relative importance of thermal versus compositional heterogeneity, *Geophysical Journal International*, 177, 1284 – 1304, doi:10.1111/j.1365-246X.2009.04133.x.

Soldati, G., L. Boschi, and A. Piersanti (2003), Outer core density heterogeneity and the discrepancy between PKP and PcP travel time observations, *Geophysical Research Letters*, 30, 1190, doi:10.1029/2002GL016647.

Stacey, F. D., and P. M. Davis (2008), *Physics of the Earth*, fourth ed., Cambridge University Press.

Stackhouse, S., and J. P. Brodholt (2007), The high temperature elasticity of MgSiO<sub>3</sub> post-perovskite, in *Geophysical Monograph: Post-Perovskite - The Last Mantle Phase Transition*, *Geophysical Monograph Series*, vol. 174, edited by K. Hirose, J. Brodholt, T. Lay, and D. Yuen, AGU.

Stackhouse, S., J. P. Brodholt, J. Wookey, J.-M. Kendall, and G. D. Price (2005), The effect of temperature on the seismic anisotropy of the perovskite and post-perovskite polymorphs of MgSiO<sub>3</sub>, *Earth and Planetary Science Letters*, 230, 1 – 10, doi:10.1016/j.epsl.2004.11.021.

Thomas, C., J.-M. Kendall, and J. Lowman (2004), Lower-mantle seismic discontinuities and the thermal morphology of subducted slabs, *Earth and Planetary Science Letters*, 225, 105 – 113, doi:10.1016/j.epsl.2004.05.038.

Tomé, C. N., and G. R. Canova (1998), Self-consistent modeling of heterogeneous plasticity, in *Texture and Anisotropy. Preferred Orientations in Polycrystals and their Effect on Materials Properties*, edited by U. F. Kocks, C. N. Tomé, and H.-R. Wenk, pp. 466

- 511, Cambridge University Press.

Tommasi, A., D. Mainprice, G. Canova, and Y. Chastel (2000), Viscoplastic self-consistent and equilibrium-based modeling of olivine lattice preferred orientations: Implications for the upper mantle seismic anisotropy, *Journal of Geophysical Research*, 105, 7893 – 7980.

Tommasi, A., A., B. Tikoff, and A. Vauchez (1999), Upper mantle tectonics: three-dimensional deformation, olivine crystallographic fabrics and seismic properties, *Earth and Planetary Science Letters*, 168(1-2), 173 – 186, doi:10.1016/S0012-821X(99)00046-1.

Tsuchiya, T., J. Tsuchiya, K. Umemoto, and Wentzcovitch (2004), Phase transition in MgSiO<sub>3</sub> perovskite in the Earth's lower mantle, *Earth and Planetary Science Letters*, 224, 241 – 248, doi:10.1016/j.epsl.2004.05.017.

Vinnik, L., B. Romanowicz, Y. Le Stunff, and L. Makeyeva (1995), Seismic anisotropy in the D'' layer, *Geophysical Research Letters*, 22, 1657 – 1660.

Walker, A. M., P. Carrez, and P. Cordier (2010), Atomic-scale models of dislocation cores in minerals: progress and prospects, *Mineralogical Magazine*, 74, 381 – 413, doi: 10.1180/minmag.2010.074.3.381.

Walte, N., F. Heidelbach, N. Miyajma, and D. Frost (2007), Texture development and TEM analysis of deformed CaIrO<sub>3</sub>: Implications for the D'' layer at the core-mantle boundary, *Geophysical Research Letters*, 34, L08306, doi:10.1029/2007GL029407.

Walte, N. P., F. Heidelbach, N. Miyajma, D. J. Frost, D. C. Rubie, and D. P. Dobson (2009), Transformation textures in post-perovskite: Understanding mantle flow in the D'' layer of the Earth, *Geophysical Research Letters*, 36, L04,302, doi:

10.1029/2008GL036840.

Wenk, H.-R., and C. N. Tomé (1999), Modeling dynamic recrystallization of olivine aggregates deformed in simple shear, *Journal of Geophysical Research*, 104, 25,513 – 25,527.

Wenk, H.-R., S. Speziale, A. K. McNamara, and E. J. Garnero (2006), Modeling lower mantle anisotropy development in a subducting slab, *Earth and Planetary Science Letters*, 245, 302 – 314.

Wenk, H.-R., S. Cottaar, C. N. Tomé, A. McNamara, and B. Romanowicz (2011), Deformation in the lowermost mantle: From polycrystal plasticity to seismic anisotropy, *Earth and Planetary Science Letters*, 306, 33 – 45, doi:10.1016/j.epsl.2011.03.021.

Wentzcovitch, R. M., T. Tsuchiya, and J. Tsuchiya (2006), MgSiO<sub>3</sub> postperovskite at D" conditions, *Proceedings of the National Academy of Science*, 103, 543 – 546.

Wookey, J., and J.-M. Kendall (2007), Seismic anisotropy of post-perovskite and the lowermost mantle, in *Post-perovskite: the last mantle phase transition*, *Geophysical Monograph Series*, vol. 174, edited by K. Hirose, J. Brodholt, T. Lay, and D. Yuen, pp. 171 – 189, AGU.

Wookey, J., and J.-M. Kendall (2008), Constraints on lowermost mantle mineralogy and fabric beneath Siberia from seismic anisotropy, *Earth and Planetary Science Letters*, 275, 32 – 42, doi:10.1016/j.epsl.2008.07.049.

Wookey, J., J.-M. Kendall, and G. Rümpker (2005a), Lowermost mantle anisotropy beneath the north Pacific from differential S–ScS splitting, *Geophysical Journal International*, 161, 829 – 838, doi:10.1111/j.1365-246X.2005.02623.x.

Wookey, J., S. Stackhouse, J.-M. Kendall, J. P. Brodholt, and G. D. Price (2005b), Efficacy of the post-perovskite phase as an explanation for lowermost-mantle seismic properties,

*Nature*, 438, 1004 – 1007.

Yamazaki, D., T. Yoshino, H. Ohfuchi, J. Ando, and A. Yoneda (2006), Origin of seismic anisotropy in the D'' layer inferred from shear deformation experiments on post-perovskite phase, *Earth and Planetary Science Letters*, 252, 372 – 378, doi: 10.1016/j.epsl.2006.10.004.

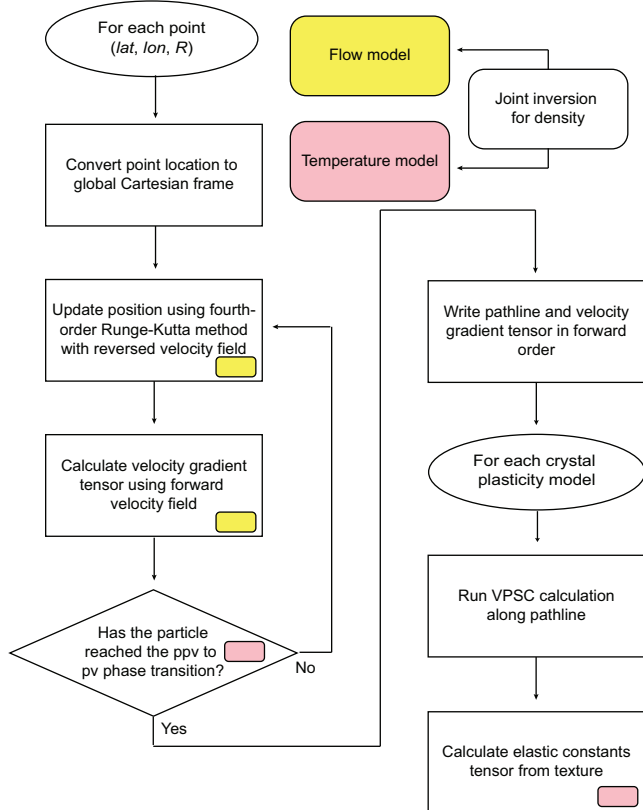


**Figure 1.** Outline of the steps taken to calculate D'' anisotropy. Use of temperature and flow fields derived from joint inversion are indicated by coloured boxes.

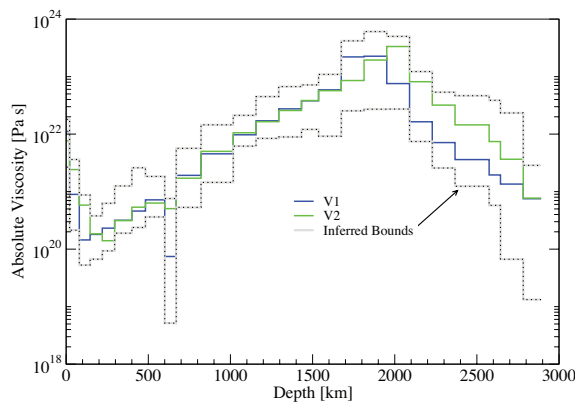


**Figure 2.** Viscosity models used to convert from density anomalies to flow velocities from the work of *Mitrovica and Forte* [2004]. V1 (blue) corresponds to the lower viscosity model and V2 (green) corresponds to the higher viscosity model.

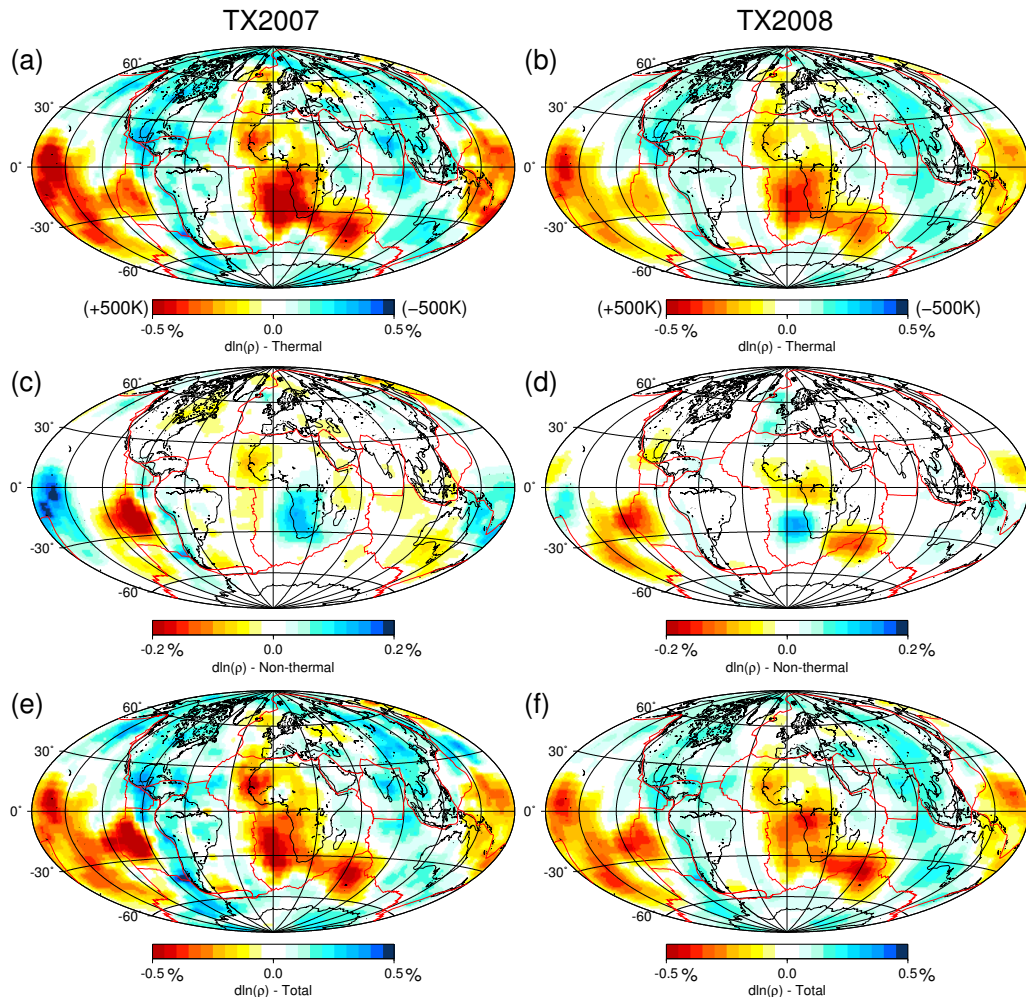


**Figure 3.** Thermal (a and b), non-thermal (c and d) and total (e and f) density anomalies for the deepest later (covering the interval from a depth of 2650 km to the CMB) in the TX2007 (a, c and e) and TX2008 (b, d and f) models.

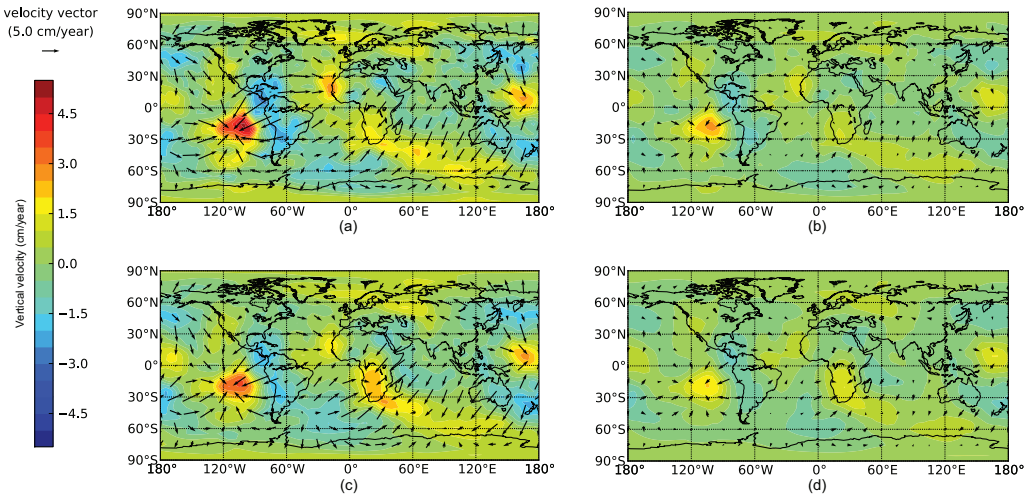


**Figure 4.** Maps showing the radial (colour) and horizontal (arrows) flow 150 km above the CMB for the four flow fields used in this study. (a) TX2007.V1; (b) TX2007.V2; (c) TX2008.V1; (d) TX2008.V2. Note that the vertical and horizontal velocity shown in parts (a) and (c) (left hand side) is approximately double that of (b) and (d) (right hand side) and that the horizontal velocity generally dominates.

**Table 1.** Slip system activities used for VPSC calculations. Plasticity model P100 uses the parameters of *Merkel et al.* [2007] which favour slip on the {011} and (100) planes. P010 is taken from the Peierls-Nabarro modelling of *Carrez et al.* [2007a, b] and *Metsue et al.* [2009] and favours slip on the (010) plane. P001 is intended to favour slip on the (001) slip as observed by *Miyagi et al.* [2010].

Slip system	P100	P010	P001
[100](001)	10	2.6	1
[010](001)	10	4.1	1
[001](010)	$\infty$	1.0	$\infty$
[001](100)	2	5.4	10
[010](100)	1	5.2	10
[001]{110}	4	2.9	10
$\langle 110 \rangle(001)$	10	4.1	2
[100]{011}	$\infty$	6.8	$\infty$
[100](010)	$\infty$	4.7	$\infty$
$\langle 110 \rangle\{110\}$	1	8.8	10

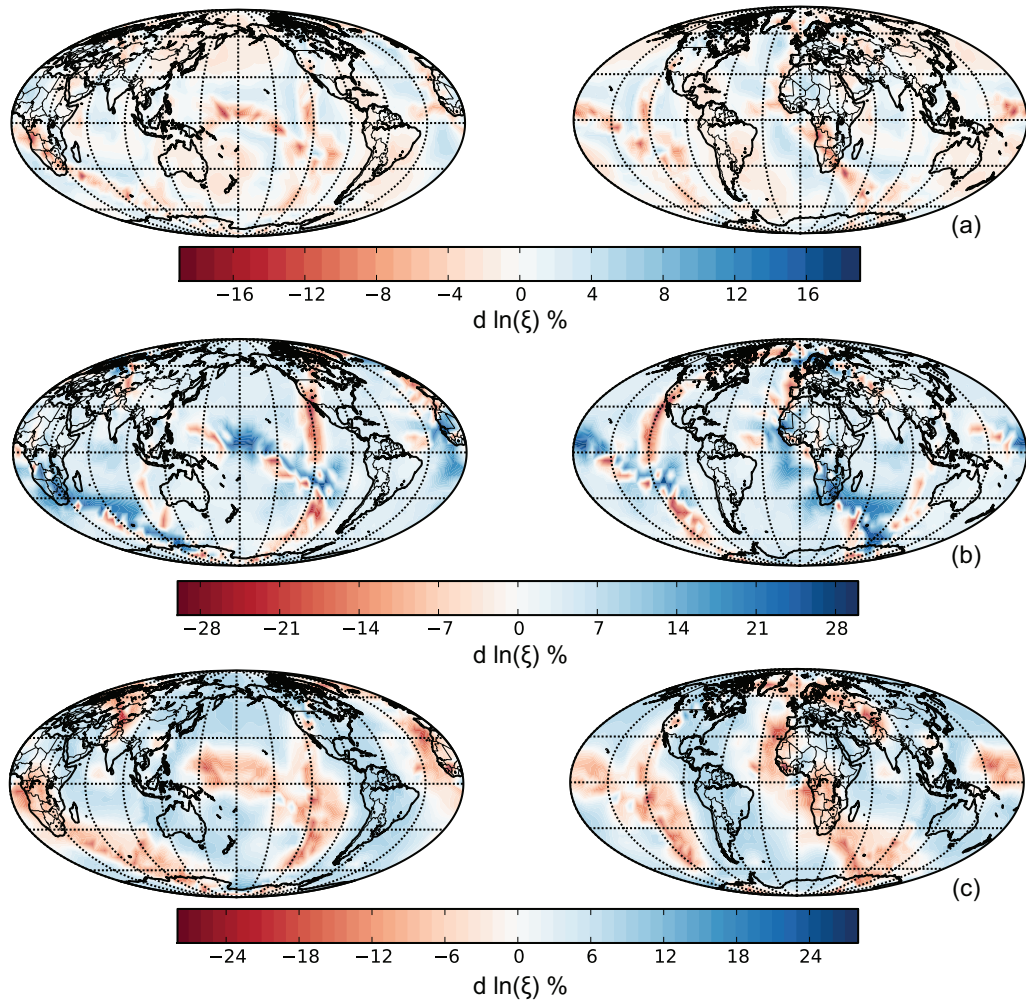


**Figure 5.** Calculated anisotropy, expressed as  $\ln(\xi)$ , for flow model TX2008.V1 75 km above the CMB with a temperature independent perovskite to post-perovskite phase transition 150 km above the CMB and three different single crystal plasticity models favouring dislocation motion on (010), (001) and (100). (a) TX2008.V1.P010, (b) TX2008.V1.P001, (c) TX2008.V1.P100.

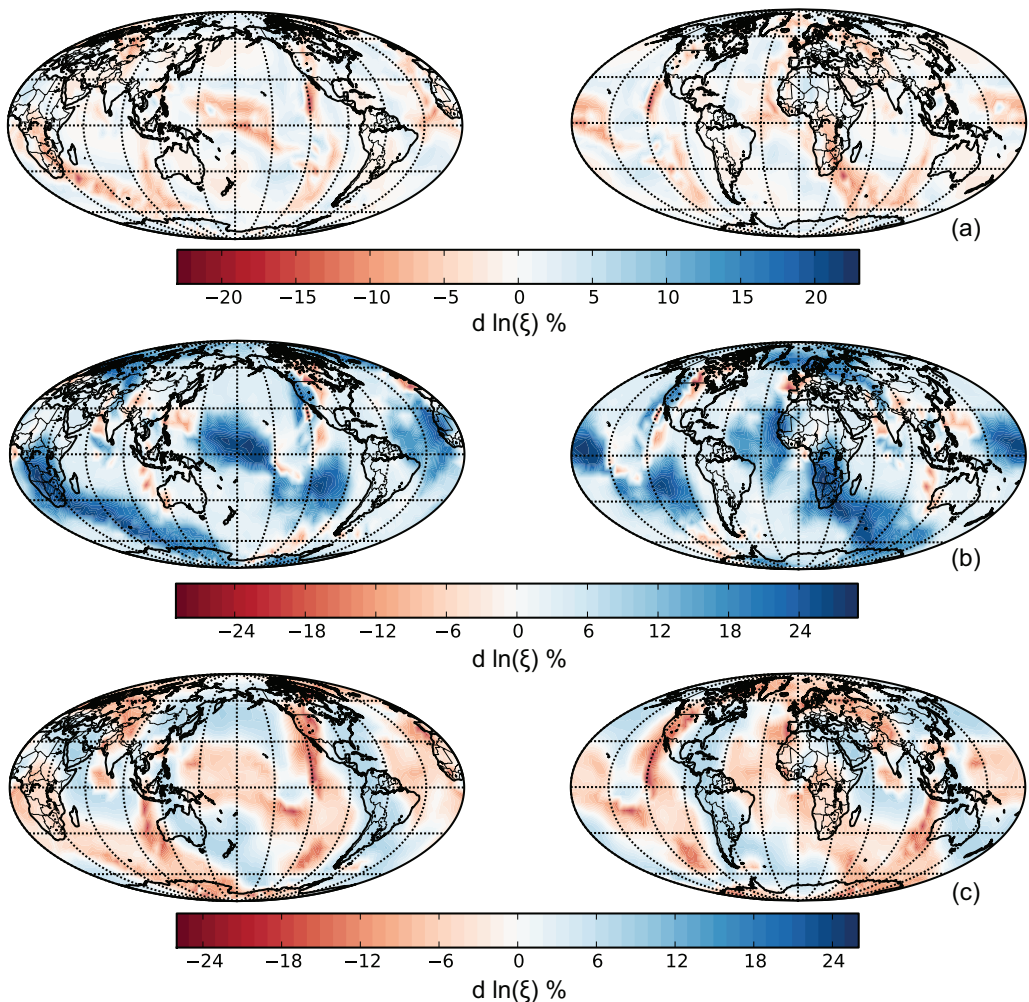


**Figure 6.** Same as Figure 5 but for a flow model with higher-viscosity lower mantle flow model TX2007.V2. (a) TX2008.V2.P010, (b) TX2008.V2.P001, (c) TX2008.V2.P100.

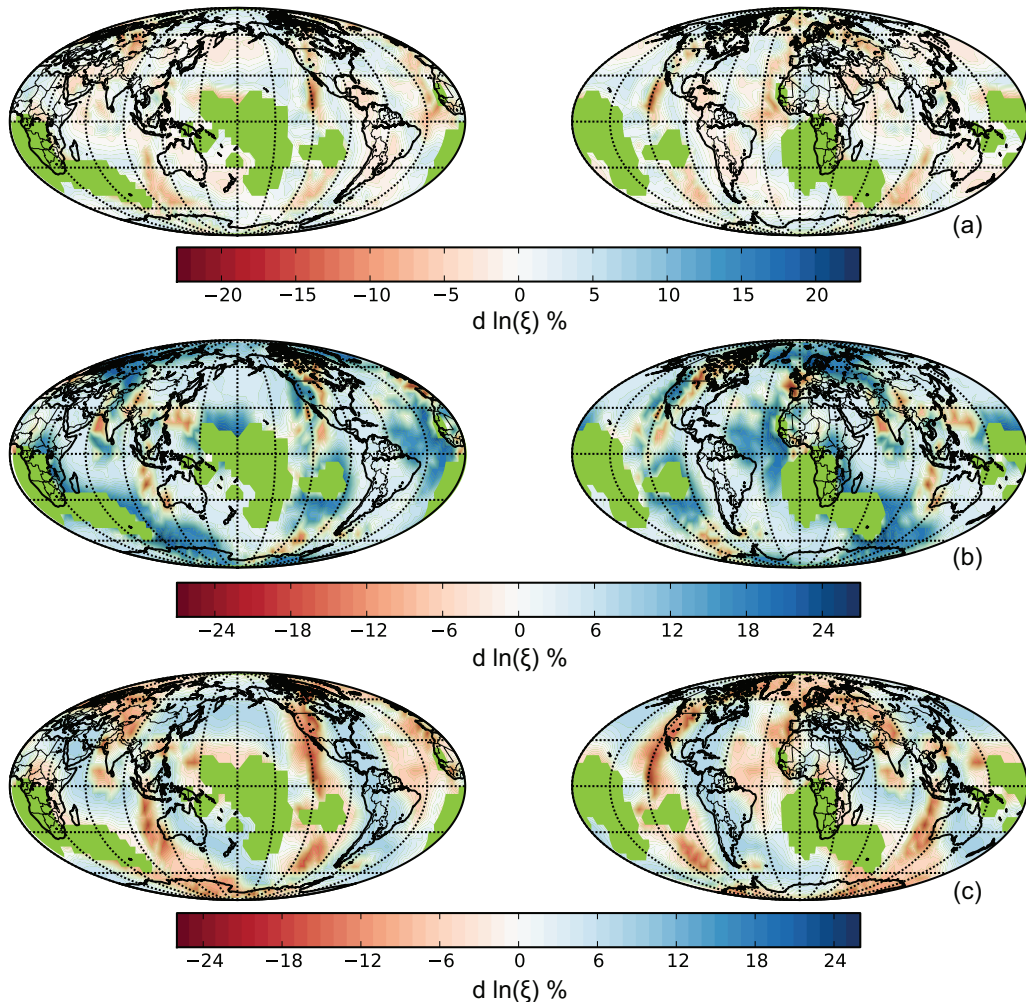


**Figure 7.** Same as Figure 6 but with thermally induced topography included on the perovskite to post-perovskite phase transition. Regions where points 75 km above the CMB are outside the post-perovskite stability field for the thermal and thermodynamic model described in the text are shown in green. A thinner layer of post-perovskite exists under most of these areas. (a) TX2008.V2.T.P010, (b) TX2008.V2.T.P001, (c) TX2008.V2.T.P100

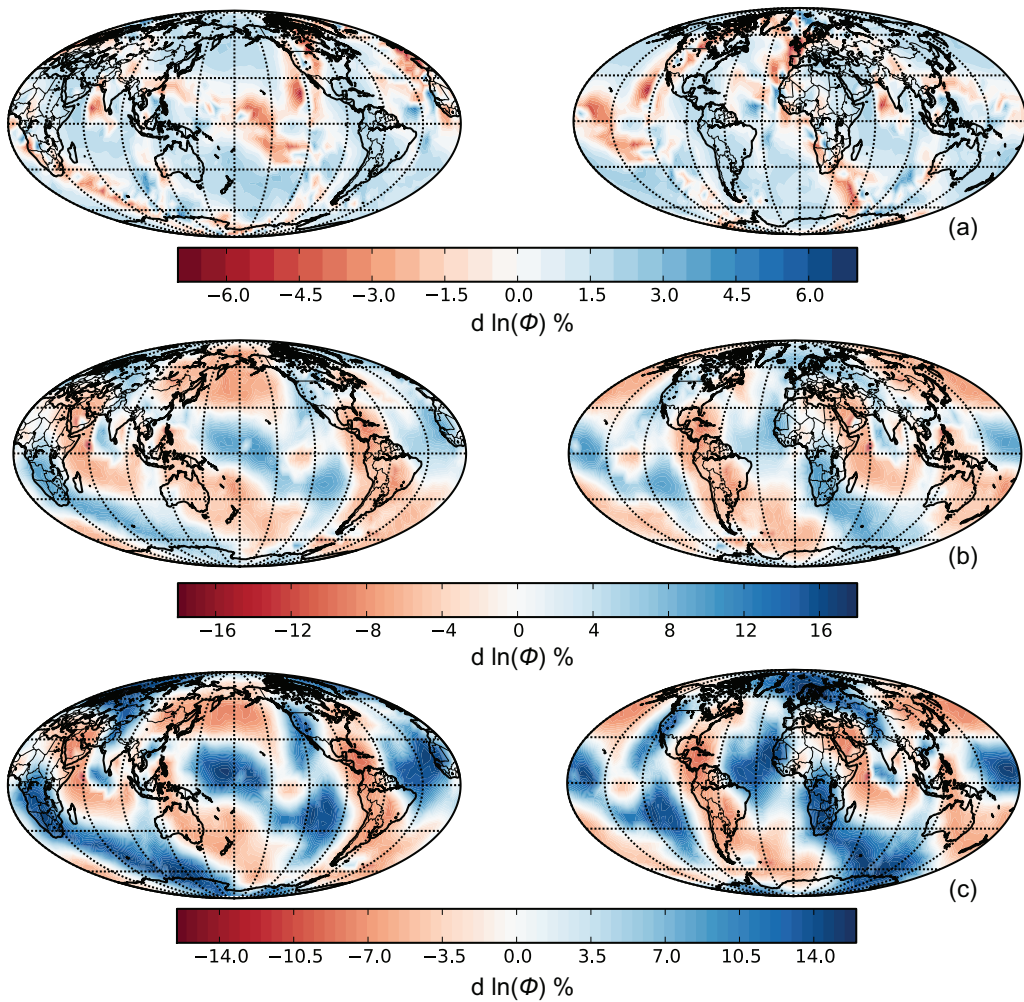


**Figure 8.** Calculated P-wave anisotropy 75 km above the CMB, expressed as  $\ln(\phi)$ , for flow model flow model TX2008.V2 with a temperature independent perovskite to post-perovskite phase transition 150 km above the CMB and three different single crystal plasticity models favouring dislocation motion on (010), (001) and (100). (a) TX2008.V2.P010, (b) TX2008.V2.P001, (c) TX2008.V2.P100.

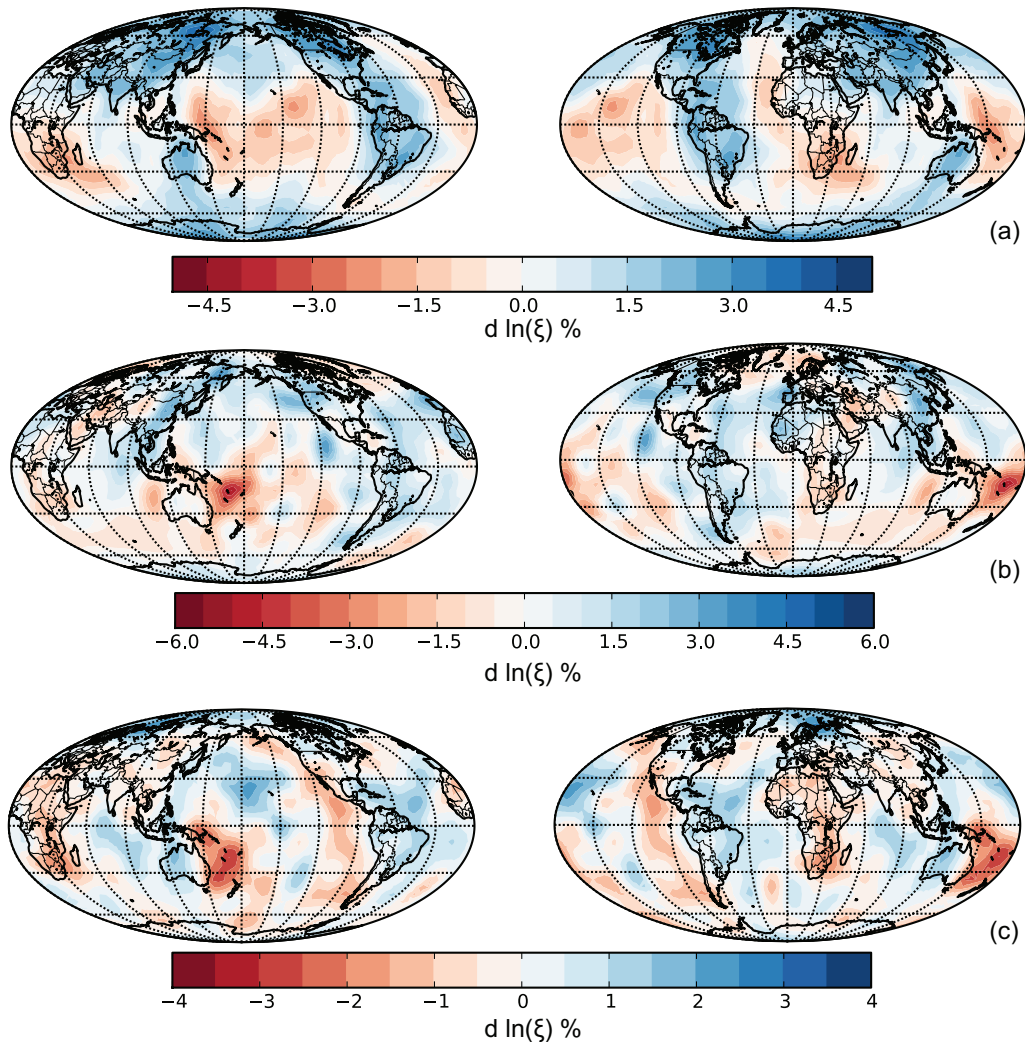


**Figure 9.** Three models of D'' anisotropy 75 km above CMB from global tomography (a) SAW642AN [Panning and Romanowicz, 2006], (b) S362WMANI [Kustowski et al., 2008], (c) SAW642ANb [Panning et al., 2010].

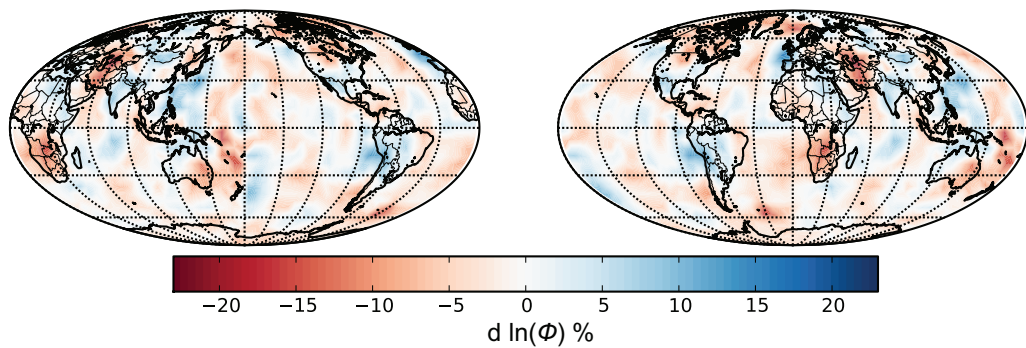


**Figure 10.** P-wave anisotropy of the 193.3 km thick lowermost mantle layer of the SBP03 [Soldati *et al.*, 2003] global tomographic model.

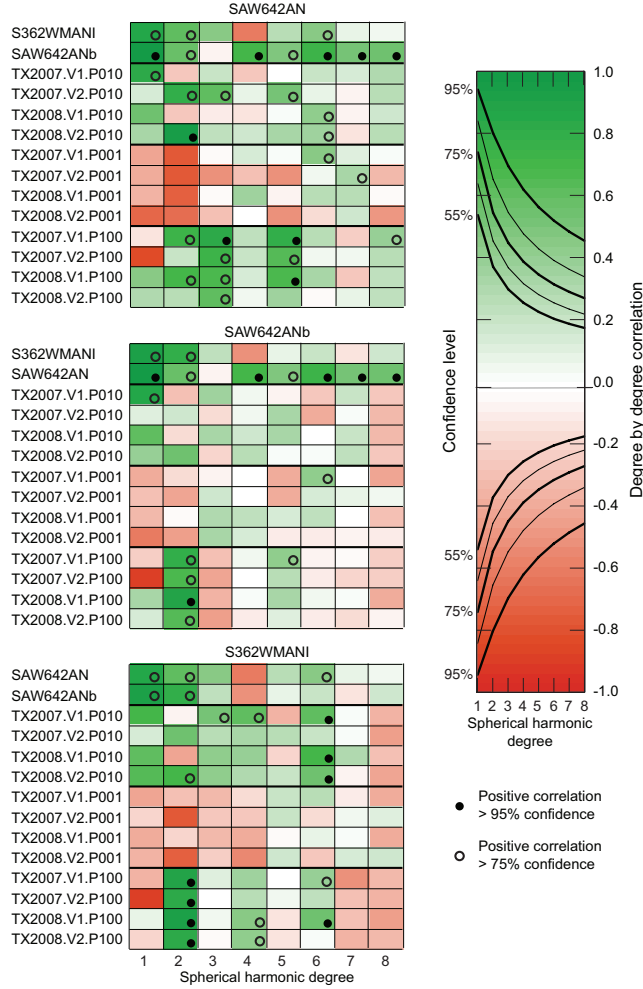


**Figure 11.** Degree by degree correlation spectra comparing the three tomographic models SAW642AN [Panning and Romanowicz, 2006], SAW642ANb [Panning et al., 2010] and S362WMANI [Kustowski et al., 2008] with each other and with the twelve combinations of mantle flow and single crystal plasticity models 75 km above the CMB. A correlation of 1 indicates complete correlation at the particular spherical harmonic degree, 0 shows no correlation, and  $-1$  is anti-correlated. The confidence that can be assigned to any given correlation is dependent on the spherical harmonic degree as shown by lines in the legend. Positive correlation at  $> 95\%$  and  $> 75\%$  confidence is highlighted.

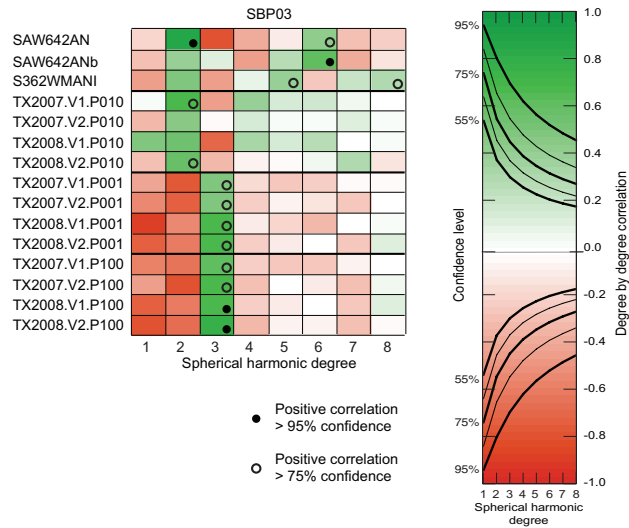


**Figure 12.** Degree by degree correlation spectra comparing the lowermost layer of the SBP03 P-wave tomographic model [Soldati *et al.*, 2003] with each of the three S-wave tomographic models, SAW642AN [Panning and Romanowicz, 2006], SAW642ANb [Panning *et al.*, 2010] and S362WMANI [Kustowski *et al.*, 2008], and with the twelve combinations of mantle flow and single crystal plasticity models, 75 km above the CMB.

**Table 2.** Summary parameters of the calculated elastic anisotropy 75 km above the CMB. The non-VTI component of the elastic constants tensors are evaluated from the norms or the total anisotropic tensor projected onto the isotropic, hexagonal, tetragonal, orthorhombic, monoclinic and triclinic components [Browaeys and Chevrot, 2004, equation 4.1]; the isotropic and hexagonal components contribute to the vertical transverse isotropy and the sum of the remaining components are reported in the table. SAW642AN, S362WMANI and SAW642ANb refer to the global anisotropic tomography results of *Panning and Romanowicz* [2006], *Kustowski et al.* [2008] and [*Panning et al.*, 2010], respectively.

	ln( $\xi$ ) (%)			non-VTI (%)		
	min	mean	max	min	mean	max
TX2007.V1.P100	-26.6	1.3	14.2	0.7	5.1	13.1
TX2007.V2.P100	-23.1	-1.9	12.7	1.0	6.2	13.0
TX2008.V1.P100	-26.6	1.3	14.2	0.8	4.9	12.0
TX2008.V2.P100	-25.6	-1.5	9.2	1.0	6.0	12.4
TX2008.V2.T.P100	-25.6	-0.9	10.7	0.3	7.2	12.4
TX2007.V1.P010	-20.1	-0.3	8.2	0.4	2.7	19.3
TX2007.V2.P010	-15.9	-0.6	7.8	0.5	3.1	9.8
TX2008.V1.P010	-19.5	-0.4	7.8	0.5	2.4	9.1
TX2008.V2.P010	-22.1	-0.2	8.7	0.5	3.1	11.8
TX2008.V2.T.P010	-22.3	-0.2	9.3	0.5	4.2	10.8
TX2007.V1.P001	-28.5	3.1	28.1	0.6	7.1	14.1
TX2007.V2.P001	-29.1	8.1	28.7	0.7	7.5	14.2
TX2008.V1.P001	-29.2	3.4	28.2	0.6	6.8	14.2
TX2008.V2.P001	-28.8	7.8	28.2	0.8	7.5	14.0
TX2008.V2.T.P001	-28.0	10.5	28.2	2.3	9.6	14.2
SAW642AN	-2.5	1.0	4.1	—	—	—
S362WMANI	-5.0	0.2	3.7	—	—	—
SAW642ANb	-3.0	0.2	2.6	—	—	—

**Table 3.** Summary parameters of the pathlines calculated for the combinations of density, viscosity and phase transition models used. The speed is measured at each point on each pathline calculated for each flow model, the path length is the sum of the straight line distance between each point on each path and the tortuosity is the ratio of this length to the straight line distance between the start and end of the pathline. A straight pathline thus has tortuosity of 1 while a semicircular pathline  $\frac{1}{2}\pi \sim 1.57$ .

	TX2007.V1	TX2007.V2	TX2008.V1	TX2008.V2	TX2008.V2.T
Maximum speed (cm/year)	17.16	9.83	12.73	7.57	6.30
Minimum speed (cm/year)	0.15	0.01	0.21	0.11	0.65
Maximum path length (km)	6525.2	5386.8	6118.5	4944.4	4205.13
Mean path length (km)	1285.5	1191.7	1315.9	1219.8	1209.44
Minimum path length (km)	74.1	75.9	73.8	75.2	3.8
Maximum tortuosity	1.78	1.56	1.48	1.62	1.52
Mean tortuosity	1.03	1.03	1.03	1.03	1.03
Minimum tortuosity	1.00	1.00	1.00	1.00	1.00